Proc. Vth International Workshop, Advances in Signal Processing for Non Destructive Evaluation of Materials
Québec City (Canada),2-4 Aug. 2005. © X. Maldague ed., É. du CAO (2006), ISBN 2-9809199-0-X

The Use of Locally Weighted Regression for the Data Fusion with Dempster-Shafer Theory

by Z. Liu, D. S. Forsyth, S. M. Safizadeh,
M.Genest, C. Mandache, and A. Fahr

Structures, Materials Performance Laboratory, Institute for Aerospace Research, National Research Council Canada, Montreal Road 1200, Ottawa, Ontario, K1A0R6, Canada

Abstract

The Dempster-Shafer (DS) theory provides an efficient framework to implement multi-sensor data fusion. Both the flexibility and the difficulty consist in defining the probability mass function. The fusion result is a discrete value or a label, which is determined by the corresponding maximum probability values. However, in some applications a continuous result is expected. In this paper, a scheme based on DS reasoning and locally weighted regression is proposed to fuse the data obtained from aircraft corrosion damage inspections. The proposed approach implements a pairwise regression that is optimized by the DS method when multiple inputs are involved. Experimental results on the fusion of conventional eddy current and pulsed eddy current data for the application of aircraft corrosion quantification are presented.

Keywords: Dempster-Shafer theory, data fusion, corrosion quantification, local weighted regression, classification

1. Introduction

The Dempster-Shafer theory has been used to fuse the data from multiple sensing modalities in various applications. The uncertainty of the measurements is modeled with the probability mass function, which defines a value between zero and one (basic probability assignment) to indicate the degree of support for a proposition [1]. In the framework provided by DS theory, the frame of discernment (θ) consists of 2^{θ} singletons, which are based on θ mutually exclusive and exhaustive propositions. In practical applications, such proposition is expressed as a discrete value or pre-defined class number to describe certain condition or status. However, not all the applications fit into this framework. For example, the quantification of corrosion damage in aircraft lap joints employs a continuous value to represent the material loss. The material loss by layer serves as one of the corrosion metrics for structural integrity and life prediction analysis [3]. Usually, the quantifying procedure is implemented by using the calibration results represented by a calibration curve. Only the first-layer corrosion can be characterized with the calibration method. Meanwhile, the problem of superimposed corrosion between multiple layers can not be solved.

The idea of fusing multiple nondestructive inspection (NDI) data is to characterize different corrosion with integrated features from multiple sources [4, 5]. The fusion operation should optimally map those features to the target outputs. In this paper, a locally weighted regression (LWR) is used with the DS approach to estimate the material loss in aircraft lap joints due to corrosion damage. In the proposed scheme, the NDI measurements are first discriminated with trained classifiers. The classification results are further combined based on the DS rule. Finally, the outputs are quantified with the LWR method for the thickness estimation. The result is compared with the "ground truth" data from the teardown inspection of a naturally corroded specimen from a service-retired aircraft. The feasibility of the proposed approach is demonstrated in this paper.

2. The approach

2.1 The general data fusion procedure

The flowchart in *Figure 1* depicts the procedure of the data fusion scheme. The estimation is carried out based on the previous available knowledge or data, which is named as the training data. The optimal number of clusters for the training data is found by using fuzzy k-means clustering and cluster validation indexes [6, 7]. Proper classifiers are assigned to the eddy current (ET) and pulsed eddy current (P-ET) data based on the cross-validation test results. The labelled training data is used to train the specific classifiers for ET and P-ET inputs respectively. The classified results determine the "data class" while the labelled X-ray data set defines the "information class". The probability mass function is defined based on the relation between these two classes.

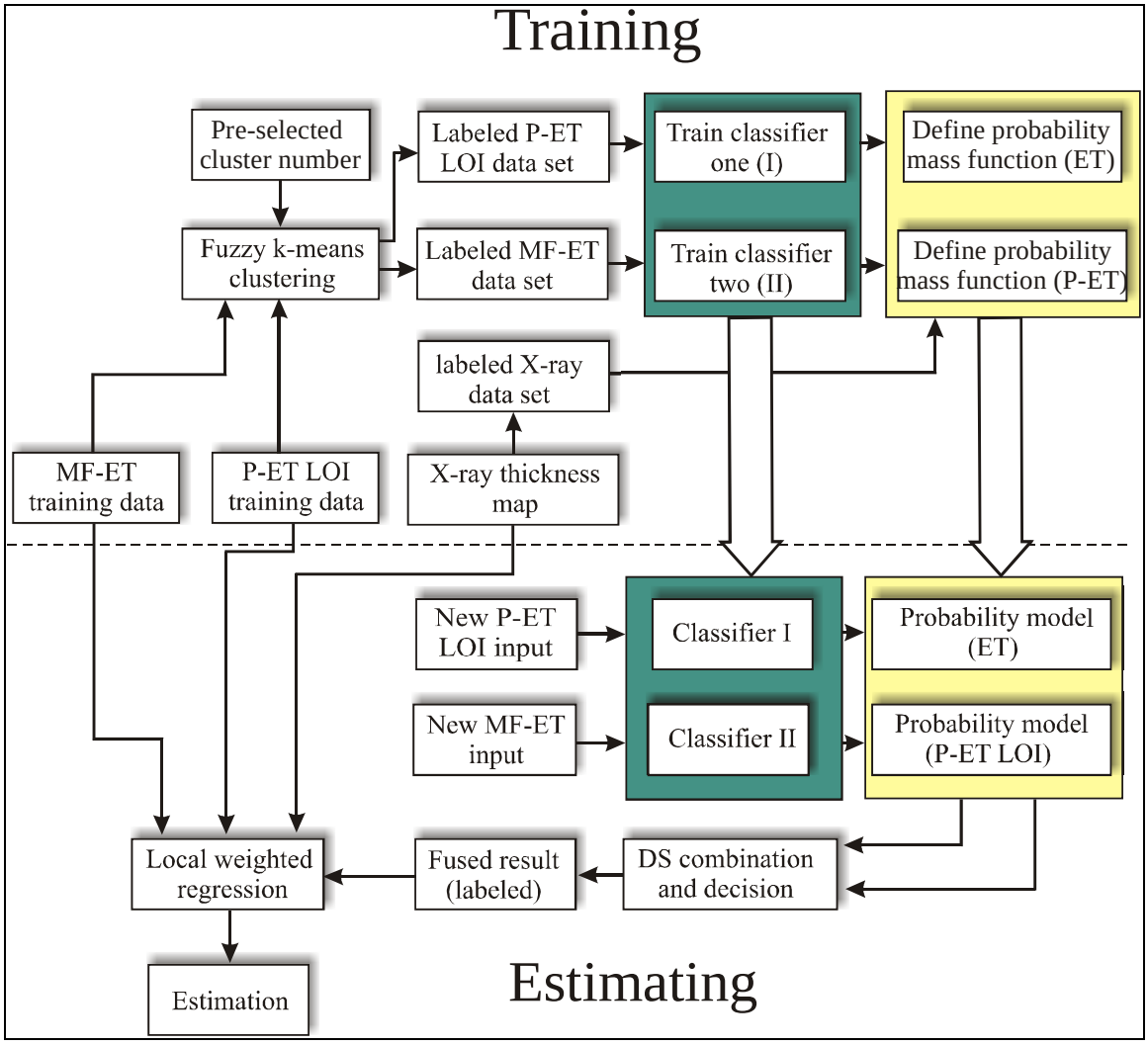

Figure 1. The data fusion procedure.

When a prediction is carried out on a new NDI measurement, the trained classifiers are applied to assign the input a pre-defined data class number. The probability mass value is derived from the probability model established during the training process. The DS combination rule fuses the

probability values and a decision is made on the maximum mass output. The regression is implemented with only the corresponding data points defined by this information class. Therefore, a continuous estimation result together with a belief value can be achieved.

2.2 Definition of probability mass function

Assuming that C_i ($i = 1,2,...,N$) represents the information class (corrosion types) and $\vec{x}$ is the vector of the measurement values, the mass value can be defined as the probability of being certain information class based on the statistical information from available training data sets, i.e. $m_s(C_i) = p(C_i|\vec{x})$ [8]. Herein, s indicates the different data sources ($s = 1,2,...,S$). The input $\vec{x}$ is mapped to data class d_j ($j = 1,2,...,M$) by a classification operation. Thus, the basic probability assignment (BPA) is defined as:

$$m_s(C_i) = p(C_i|d_j)p_s(d_j|C_i) \tag{1}$$

The second value $p_s(d_j|C_i)$ is regarded as a measurement of the capability of each data source for discriminating the information classes. According to DS theory, the BPA values must be normalized to meet the requirement $\sum_i m_s(C_i) = 1$ before the updating operation is applied.

2.3 Locally weighted regression

The local regression is estimating the value using information pertaining only to a neighborhood of the input query [9]. Supposing that the variable $y \in R$ represents the material thickness and the NDI measurement vector is $\vec{x} \in R^m$, we need to find the mapping function $f : R^m \to R$. That is:

$$y_p = f(\vec{x}_p) + \varepsilon_p \quad (p = 1,2,...,n) \tag{2}$$

Herein ε_p is a random variable. Given a query point $\vec{x}_q$, to obtain the regression applicable to this query point, the following cost function is minimized:

$$J = \sum_{p=1}^{n} \left(\beta^T \mathbf{x}_{p,1} - y_p\right)^2 K\left(\frac{|\vec{x}_q - \vec{x}_p|}{h}\right) \tag{3}$$

where, $K(\cdot)$ is a weight function and h is the bandwidth. $\mathbf{X}$ is matrix of data samples with $[\vec{x}_p, 1]^T$ in the p[th] row and $\mathbf{y} = [y_1, y_2, \cdots, y_n]^T$. The solution to the above cost function is [9]:

$$\hat{\beta} = (\mathbf{Z}'\mathbf{Z})^{-1}\mathbf{Z}'\mathbf{v} \tag{4}$$

where $\mathbf{Z} = \mathbf{WX}$ and $\mathbf{v} = \mathbf{Wy}$. $\mathbf{W}$ is a diagonal matrix with the i[th] diagonal element $w_{ii} = \sqrt{K(|\vec{x}_p, \vec{x}_q|/h)}$. The estimation at $\vec{x}_q$ is then given by : $\hat{y}(\vec{x}_p) = \hat{\beta}\vec{x}_p$.

3. Experimental results

Data sets from the inspection of a service-retired Boeing 727 aircraft are used in the experiment. A two-layer lap joint cut out from below the cargo floor was inspected by the multi-frequency eddy current testing at 5.5kHz, 8kHz, 17kHz, and 30kHz frequencies and the pulsed eddy current testing. The P-ET lift-off-intersection (LOI) scan is extracted and used for analysis [11]. The ground truth data is obtained by using digital X-ray mapping technique on each layer. Data from two sections are used for training and testing respectively. The ET data obtained at 17kHz and 30kHz together with P-ET LOI are used for the first layer thickness estimation.

The ET and P-ET data are clustered by applying the fuzzy k-means clustering algorithm. The initial cluster number is set from 2 to 14. The clustering partition index, separation index, Xie and Beni's index, and Dunn' s index are considered to select a proper cluster number for NDI data. Consequently, ET and P-ET data are clustered into 7 and 8 groups. Therefore, the X-ray data is segmented into seven parts based on the percentage of material loss. The clustered/labelled NDI data is used to train classifiers. To find an efficient classifier, the cross-validation test is applied to several candidate classifiers. The one with the smallest error is selected. In the experiment, the nearest mean classifier is employed for classifying ET and P-ET data. According to 2.2, the probability functions are defined for ET and P-ET data respectively as shown in *Figure 2*.

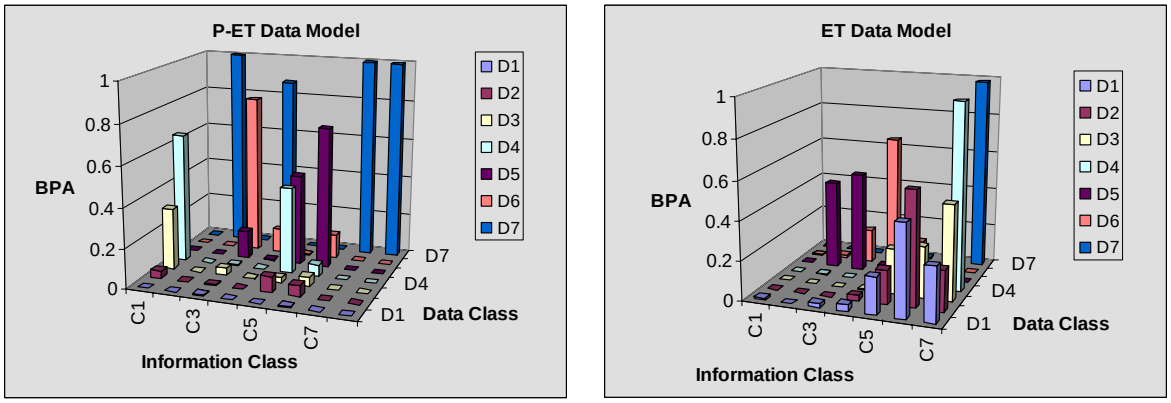

(a) (b)

Figure 2. Probability model of NDI data: (a) pulsed eddy current and (b) eddy current (17kHz and 30kHz).

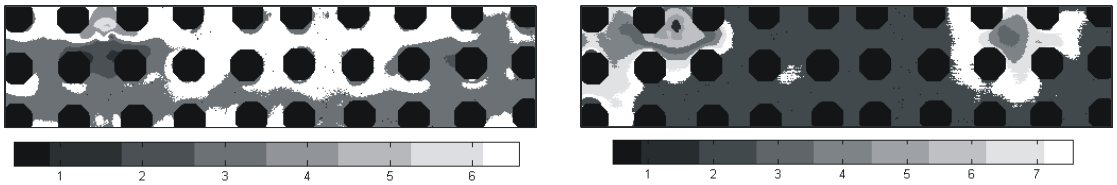

(a) (b)

Figure 3. The classification results of (a) eddy current (17kHz and 30kHz) and (b) pulsed eddy current LOI scan.

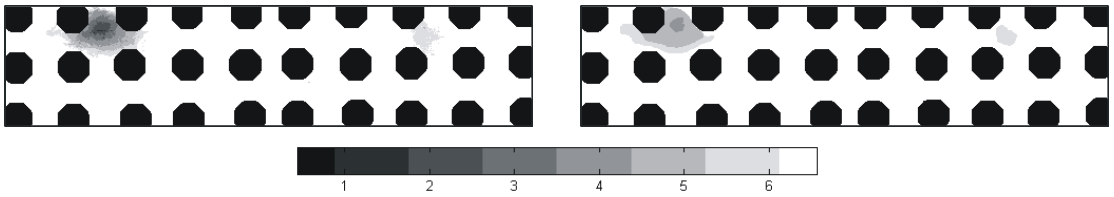

(a) (b)

Figure 4. (a) The segmentation of X-ray thickness map and (b) the fused result of Figure 2(a) and (b).

The classification results are from ET scan (17kHz and 30kHz) and P-ET LOI scan are shown in *Figure 3* (a) and (b), respectively. *Figure 4* (a) shows the segmented X-ray thickness map. The corresponding definition of the classes is given in *Table 1*. The fused result of *Figure 3* (a) and (b) is presented in *Figure 4* (b) after a morphological processing. The X-ray thickness map and the regression result can be found in *Figure 5* (a) and (b), respectively.

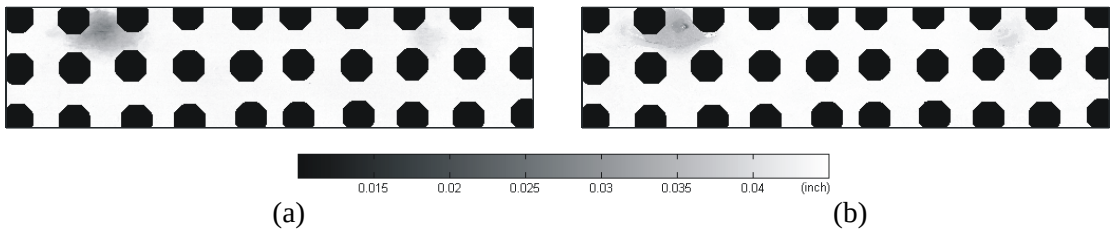

(a) (b)

Figure 5. (a) The X-ray thickness map and (b) the estimated result obtained by DS fusion and LWR.

Table 1. The definition of information classes in term of material loss (corrosion type).

Corrosion class	C1	C2	C3	C4	C5	C6	C7
Thickness range (inch)	0.024 – 0.027	0.027 – 0.030	0.030 – 0.033	0.033 – 0.036	0.036 – 0.039	0.039 – 0.042	0.042 – 0.045

Table 2. The evaluation of the fusion result.

	RMSE (E-3)	CORR	PSNR	DE	MI
ET 17kHz	1.4585	0.9992	15.0381	1.0021	0.7150
ET 30kHz	1.5017	0.9991	15.0475	0.9657	0.7157
P-ET LOI	2.4106	0.9977	16.4591	0.6286	0.8170
Fusion result	0.8151	0.9997	36.0737	0.0673	0.7939

The fusion result is compared with the X-ray thickness reference in terms of a number of image comparison metrics listed in *Table 2*, i.e. root mean square error (RMSE), cross-correlation (CORR), peak signal-to-noise ratio (PSNR), difference entropy (DE), and mutual information (MI) [10]. The DS-based fusion followed by LWR process achieves the best result. The output of DS fusion as shown in *Figure 6* can be used as an indication of the degree to which we can trust the result.

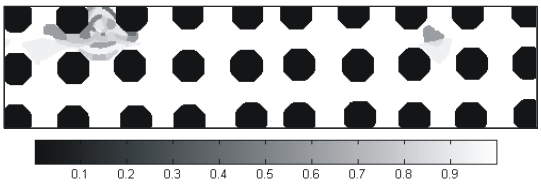

Figure 6. The DS fusion output.

4. Discussion

The result obtained in this experiment for the first-layer thickness estimation is better than the results reported previously [5]. The fusion algorithm developed here can also be applied to the deep-layer thickness estimation. However, the capability of P-ET technique for revealing and discriminating deeper layer corrosion has not been fully explored in this work. Only LOI scan, which is a single feature point in the time domain, is employed for the analysis. Another study indicates that the LOI is not fixed and changes with the presence of different corrosion damages [11]. Therefore, using single LOI point scan might not be an optimal solution.

In the proposed scheme, the classification error of the selected classifiers is not considered in the probability model. This value indicates how much we can rely on the results of a specific classifier and the probability of a measurement belongs to certain class. On one hand, an iterative classification scheme might be helpful to reduce the classification error; on the other hand, this error can be considered when the probability model is built.

The classification-based approach as presented in [12] provides a promising solution for identifying corrosion at different layers because it is a typical classification application. How to train a classifier efficiently with limited training data still remains an unsolved problem, but the classification-based approach may lead to further improvement when new data is available. Similarly, the proposed data fusion scheme also provides a mechanism for a possible improvement.

The quantification analysis relies on artificially prepared "damages" on a calibration specimen. The calibration curve is determined by limited points. The performance of the proposed fusion algorithm can be further improved in two aspects: the accuracy of the classifier and the probability model. However, the performance does not increase with the accumulation of data because the quality of the data cannot be assured. The updating mechanisms for selecting good

data and improving the fusion analysis by using the accumulated historical data would therefore make for an interesting topic for future work.

5. Summary

In this paper, a data fusion scheme based on Dempster-Shafer theory and locally weighted regression is proposed. The measurement value is optimally classified by fusing the classification results with the DS combination mechanism. The final estimation is achieved by locally weighted regression of the pre-classified results. The data fusion method achieves a better estimation of lap joint thickness than the one obtained by calibration. For our future work, the use of multiple P-ET slices around LOI point is considered. The data fusion algorithm may be applied to these P-ET images for characterizing deep-level corrosion. This will also help to identify the contribution of the eddy current technique for the thickness estimation. Another way to improve the method is to develop a mechanism to select good data and update the model and classifiers for an improved estimation.

REFERENCES

[1] HAMID (R.). – *An Experimental Data Fusion Model for Multisensor System*. PhD. Dissertation, New Mexico State University 1989.
[2] HALL (D.). - *Mathematical Techniques in Multisensor Data Fusion*. Norwood, MA, USA, Artech House, 1992.
[3] LIU (Z.), FORSYTH (D.S.), and KOMOROWSKI (J.P.). – *Fusion of Multimodal NDI Images for Aircraft Corrosion Detection and Quantification*. Blum (R.S.) and Liu (Z.) ed. Multi-sensor Image Fusion and its Applications, p. 375-404, CRC Press, 2005.
[4] FAHR (A.), FORSYTH (D.S.), and CHAPMAN (C.E.). – *Survey of Nondestructive Evaluation (NDE) Techniques for Corrosion in Aging Aircraft*. National Research Council Canada Technical Report, LTR-ST-2238, Oct. 1999.
[5] LIU (Z.), FORSYTH (D.S.), LEPINE (B.A.), SAFIZADEH (M.S.), and FAHR (A.). – *Quantifying Aircraft Hidden Corrosion by Using Multi-modal NDI*. Thompson (D.) and Chimenti (D.) ed. Review of Progress in Quantitative NDE, Vol.23, p. 1355 – 1362, Green Bay , Wisconsin, 2003.
[6] BENSAID (A.M.), HALL (L.O.), BEZDEK (J.C.), CLARKE (L.P.), SILBIGER (M.L.), ARRINGTON (J.A.), MURTAGH (R.F.). - *Validity-Guided (re)Clustering with Applications to Image Segmentation*. IEEE Transactions on Fuzzy Systems 4:112—123, 1996.
[7] XIE (X.L.), BENI (G.A.) - *Validity Measure for Fuzzy Clustering*. IEEE Transactions on Pattern Analysis and Machine Intelligence, 13(8):841 – 847, 1998
[8] FORSYTH (D.S.), LIU (Z.), KOMOROWSKI (J.P.), and PEELER (D.). – *An Application of NDI Data Fusion to Aging Aircraft Structures*. 6th Joint FAA/DoD/NASA Conference on Aging Aircraft , San Francisco, CA, USA., Sep 2002.
[9] ATKESON (C.G.), MOORE (A.W.), and SCHAAL (S.). - *Locally Weighted Learning*. Artificial Intelligence Review, 11:11-73, 1997.
[10] XUE (Z.), BLUM (R.S.), and LI (Y.). – *Fusion of Visual and IR Images for Concealed Weapon Detection*. Proc. ISIF, p. 1198 – 1205, 2002.
[11] LEFEBVRE (J.H.V.) and DUBOIS (J.M.S.). – *Lift-off Point of Intercept (LOI) Behavior*. Thompson (D.) and Chimenti (D.) ed. Review of Progress in Quantitative NDE, Vol. 24, p. 523 - 530, 2004.
[12] SAFIZADEH (M.S.), LIU (Z.), MANDACHE (C.), FORSYTH (D.S.), and FAHR (A.). – *Intelligent Pulsed Eddy Current Method for Detection and Classification of Hidden Corrosion*. V International Workshop – Advances in Signal Processing for NDE of Materials, August 2005.

Proc. Vth International Workshop, Advances in Signal Processing for Non Destructive Evaluation of Materials
Québec City (Canada),2-4 Aug. 2005. © X. Maldague ed., É. du CAO (2006), ISBN 2-9809199-0-X

Effective compression algorithms for pulsed thermography data

by S. Lugin and U. Netzelmann

Fraunhofer-Institute for Nondestructive Testing, University Bldg.37, 66123 Saarbrücken, Germany

Abstract

Two compression algorithms for the image sequences generated by pulsed-transient thermography for non-destructive testing were developed. The first algorithm allows to balance the quality of the original measurement data reproduction against the compression ratio. This algorithm comprises a dedicated space/time mapping (STM) method and an image compression algorithm (JPEG2000). The second algorithm provides lossless reproduction of the original measurement data. This algorithm is based on a particular transformation of dynamically changing data and a lossless compression algorithm (ZIP). Both algorithms were tested on typical experimental thermography data. In both cases, the achieved compression ratios were significantly higher than those of existing algorithms.

Keywords: thermography; data compression; space/time mapping

1. Introduction

Pulsed thermography (PT) has experienced wide application during the recent years due to its unique features like: contact-free operation, capability to inspect large areas simultaneously and fastness of inspection. The technical equipment and method have now reached a stage of maturity which allows them to be used for in-line full-time quality control of components. This kind of testing allows for the detection of subsurface defects, inclusions and delaminations as well as for materials characterization [1]. The inspection usually consists of three phases:

1) *Thermal excitation*
2) *Observation of the thermal response*
3) *Data analysis*

The problem we discuss in this work concerns an efficient compression of the recorded IR image sequence as obtained after phase 2. On one hand, the reconstructed measurement data should match the original data with high accuracy, on the other hand excessive data storage volume as it might occur in 24-hours process control applications has to be avoided.

As an introduction, the raw format in which the equipment stores information is briefly described. An IR camera that is used for PT may have a temperature range from -10 °C up to 100 °C. We use a focal-plane array mid-range IR camera (AIM). The IR signal is digitized with 14 bits accuracy (digital discretization). It is assumed that the camera array has an image size of 256 x 256 pixels and stores the data as words of 16 bits. According to these characteristics the size $Size_{seq}$ of the image sequence (comprising N images in raw format) is computed as:

$$Size_{seq} = N \cdot (256 \cdot 256) \cdot 2\,bytes$$

(for example, if N=200 then $Size_{seq}$= 25 MB)

Due to the signal characteristics of the image sequence, the raw data contain a significant amount of redundant information. As the thermal response of the inspected sample may be described as a diffusion process, some images after the flash occurred, the whole sequence will always change smoothly over time, i.e., the temperature of any chosen location will not change to significant amounts between adjacent frames. Based on this property, we propose two compression algorithms for pulsed thermography data. Note that, in general, there are two kinds of data compression: lossless

compression and compression with slight losses (the latter being frequently used for the storage of images as well as audio and video data). Both paths are pursued in this work.

2. Raw measurement data format

Prior to the description of the algorithms, the raw data format as provided by the PT equipment is considered. During the measurement the IR camera generates the sequence of *S* images, each image having the same size (*M*x*N* pixels), where each image pixel is represented by a word of 16 bits. The whole sequence is stored on a media device as a single file. Further, in the paper we use the abbreviation $IM_{raw}(i,j,t)$ to address to the IR value in the point *i,j* ($1 \le i \le N, 1 \le j \le M$) at the time *t* ($1 \le t \le S$).

3. Lossy data compression

3.1 Time signal reconstruction (TSR) method

To estimate the efficiency of the algorithm proposed in the following, its results will be compared with the results of the thermographic signal reconstruction (TSR) method [2, 3] which was especially developed for pulsed thermography. The TSR method serves as a reference for the algorithm proposed in the following.

3.2 Space/time mapping JPEG-based data compression

A unique aspect of the algorithm we propose is to combine spatial and temporal information in the cooling image sequences. The main idea lies in a transformation of the recorded data $IM_{raw}(i,j,t)$ into a single image STM to be further compressed [4]. The algorithm consists of three steps:

1) *Extraction of the dynamically changing part of the data*
2) *Space/time mapping*
3) *JPEG compression*

The first and second steps were developed and described in detail in our previous work [4]. The novelty in this work is an application of the common JPEG2000 algorithm [5] for compression of the image STM. This image compression algorithm was chosen for its high compression ratio, high reconstruction quality and high speed. The algorithm accepts the *quality/size* ratio as an input parameter for the compression procedure. The range of this parameter and its influence depends on the particular implementation of the algorithm.

In our implementation of the algorithm we used the programming language LabVIEW to produce the image STM as a BMP file and the image processing package Corel PHOTO-PAINT to compress it. The package provides JPEG2000 compression as a function of exporting that requires an input parameter *CMP* in the range 1-100 for varying the *quality*/*size* ratio. The value 1 corresponds to high quality at low compression, and the value 100 corresponds to low quality at high compression.

In section 3.3 we present the results of pulsed thermography data compression for several values of *CMP*.

3.3 Compression results

In most the STM-JPEG algorithm compressed data tightly and provided high reproduction quality. In the following, results are presented of two example IR image sequences compressed with different values of *CMP*. The quality and file size are compared to those obtained by use of the TSR method. A parameter *RL* is used as a measure for reproduction loss estimation:

$$RL = \frac{1}{MN} \sum_{i}^{N} \sum_{j}^{M} RMSE_{ij} , \qquad (1)$$

where $RMSE_{ij}$ is the root mean square error computed against the actual cooling curve at the point *i,j* of the image sequence:

$$RMSE_{ij} = \sqrt{\frac{1}{S}\sum_{t}^{s}\left(IM_{raw}(i,j,t) - IM_{rep}(i,j,t)\right)^2} \quad , \tag{2}$$

where $IM_{rep}(i,j,t)$ is a pixel with the coordinates *i,j* in the image number *t* of the decompressed image sequence.

Remark: In order to suppress image noise which is inevitable under practical circumstances, a 3 x 3 median filtering was applied to the measured data before storing them in raw format.

In the first example, a polyvinylchloride (PVC) plate (thickness: 1 cm) containing two lengthy grooves simulation sub-surface defects (depths: 0.7 mm and 1 mm) was tested. Flash lamp heating was employed. The image sequence included 188 images with a size of 256 x 256 pixels. The data in the centre region of interest (128 x 128 pixels) were extracted and stored in raw format, which required 5.9 MB of storage space. Further the data were compressed by TSR and the STM-JPEG algorithm and their reproduction estimated by Eq. (1). Table 1 shown below summarizes the result of compression at different values *CMP* of the JPEG compression.

Table 1. Compression results on a PVC plate with buried grooves

Factor	TSR method	STM-JPEG algorithm				
		CMP=1	*CMP*=20	*CMP*=40	*CMP*=60	*CMP*=80
Size, KB	320	314	241	139	77	32
Reproduction losses (*RL*)	5.95	2.79	3.14	3.84	4.55	5.50

The STM-JPEG compressed file size can be one tenth of that of the TSR method, or to a total compression factor of 184 at *CMP*=80. At the same *CMP*, the reproduction losses are still at a lower level than for TSR. In a trade-off with file size, *RL* can be made significantly smaller. This may be helpful, if defect reconstruction algorithms will be applied on the IR data.

In the second example, the object under test was a sample made from polyethylene which contained 4 circular defects of different diameters in different depth (diameter/depth: 3/1.2 mm, 5/1 mm, 3/2 mm and 5/2 mm). The results are similar to that of the first example. Fig. 1(a) shows a thermographic image of the test specimen from the cooling sequence. The entire sequence contained 98 images with a frame spacing of 0.35 s.

Again, the centre region of 128 x 128 pixels was extracted and stored in raw data format (3 MB). The compression results are shown in Table 2.

Table 2. Compression results on a polyethylene sample with flat bottom holes

Factor	TSR method	STM-JPEG algorithm				
		CMP=1	*CMP*=20	*CMP*=40	*CMP*=60	*CMP*=70
Size, KB	320	226	183	134	82	59
Reproduction losses (*RL*)	5.02	2.49	2.81	3.29	4.03	4.55

The reproduction losses are shown in Fig. 1(b,c) for the reference algorithm (TSR) and the STM-JPEG algorithm proposed here. The grey values represent the $RMSE_{ij}$ as defined in Eq. (2). A perfect reconstruction would produce a black image. It is obvious that the proposed algorithm reduces the reproduction error significantly, in particular at the defect positions.

4. Lossless data compression

The problem of lossless data compression has been widely discussed. The most famous algorithms developed for solving this problem and using nowadays are Huffman coding, LZW coding and arithmetic coding [6].

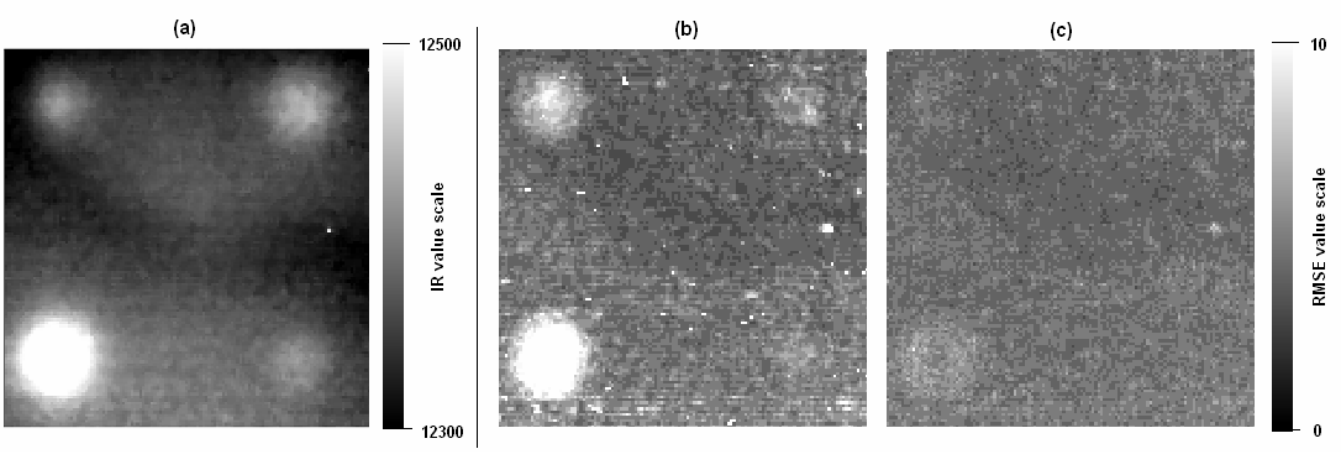

Fig. 1 (a) - Thermographic image (frame 40) from the cooling sequence. The four sub-surface defects are visible close to the corners (image size 37 mm x 37 mm). (b,c) Images of the reproduction loss obtained by both algorithms ((b) - TSR method, (c) - STM-JPEG compression at *CMP*=70), the grey values represent the $RMSE_{ij}$ as defined in Eq. (2).

These algorithms are based on different approaches but have in common that they exhibit a dependence of the compression ratio on the data to be compressed. A data block having a high number of repetitions can be compressed tighter than a data block having a low repetition number. In some cases the transformation of a source data block based on the information context allows to intentionally increase the number of repetitions and in consequence, to increase the compression ratio. Considering pulsed thermography data in the raw format one can note that there are few repetitions, so this does not allow to achieve a high compression ratio using existing algorithms. As an approach to this problem, it is necessary to transform the data into a form suitable for compression. In this work we propose an algorithm that consists of a dynamically changing data transformation (DCDT) of measurement data and a compression package (ZIP) chosen as a widespread lossless compression package.

To compress pulsed thermography data, the algorithm performs three steps:

1) *Transformation of dynamically changing data (DCDT)*
   The algorithm separates dynamical and statical information, stores the data in the form suitable for compression.
2) *Lossless compression*
   The transformed data is compressed by the ZIP algorithm.

4.1 Transformation of dynamically changing data

In this step the algorithm separates dynamical and statical information the data contains. As statical information, the average cooling process is considered. All image IR values $IM_{raw}(i,j,t)$ at $1 \le t \le S$ decrease with more or less similar speed that is explained by a transient cooling process after thermal excitation. To separate the cooling process and dynamical changes (dc), the algorithm computes average image temperatures *AV(t)*:

$$AV(t) = \left[\frac{\sum_i \sum_j IM_{raw}(i,j,t)}{MN} \right], \tag{3}$$

and subtracts the computed temperatures from source images:

$$IM_{dc}(i,j,t) = IM_{raw}(i,j,t) - AV(t). \tag{4}$$

The row *AV(t)* represents the average process of cooling while the values $IM_{dc}(i,j,t)$ describe the thermal dynamic changes caused by internal thermal reflections. Further the algorithm extracts dynamic changes of single image pixels (sip) computing the difference of pixel values between adjacent images:

$$IM_{dc-sip}(i,j,t) = IM_{dc}(i,j,t) - IM_{dc}(i,j,t+1) \quad (5)$$

Note that the difference $IM_{dc\text{-}sip}(i,j,t)$ is computed for all pixel values except the last image *S*. The performed computations significantly increase numbers of repetitions in the data $IM_{dc\text{-}sip}(i,j,t)$. If the probability histogram of $IM_{dc\text{-}sip}(i,j,t)$ is considered, the maximal probability will be close to 0 and rapidly decrease from 0 to $+\infty$ and from 0 to $-\infty$. In binary form it has a following feature that bits of low order contain most of changes while bits of high order almost always equal to zero. In order to effectively use this feature, the algorithm carries out a bit separation by bit order. Note, that we choose 16-bits integer form to store values $IM_{dc\text{-}sip}(i,j,t)$ where the highest bit is used for a sign and 15 bits are used for the number coding. The algorithm forms 16 single data chains by the following equation:

$$DC(n) = \perp_t \perp_i \perp_j \left(IM_{dc-sip}(i,j,t)_{[n]}\right) \qquad \textit{for n=0…15} \quad (6)$$

where the abbreviation $IM_{dc-sip}(i,j,t)_{[n]}$ denotes an extraction of the n-th bit from the value $IM_{dc-sip}(i,j,t)$ and the abbreviation $\perp_k a(k)$ denotes a bit concatenation of elements a in forward order: $a(1), a(2), a(3)\ldots$. This transformation is schematically shown in Fig 2. To store data chains, they are converted in the byte form.

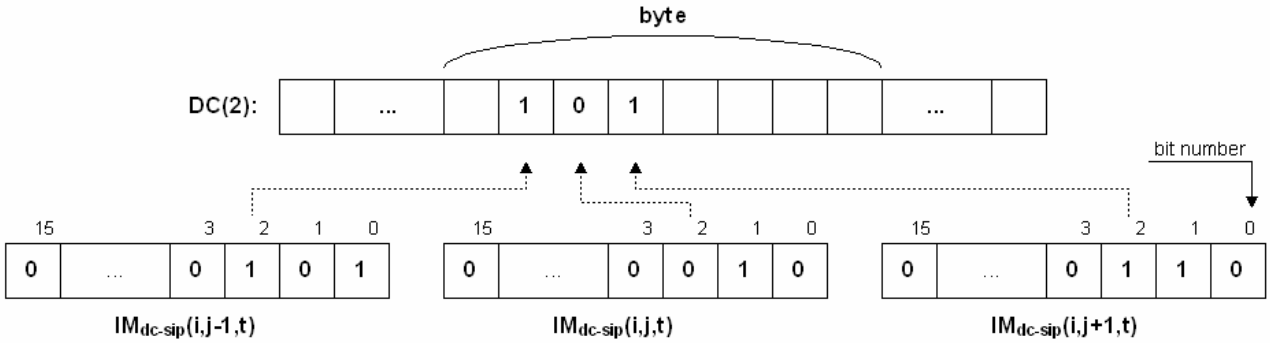

Fig. 2. Example of the formation of the data chain *DC(2)*

After these steps have been done, the algorithm stores a data structure that includes the raw *AV(t)*, the last image $IM_{dc}(i,j,S)$, and 16 data chains *DC(n)*. For simplicity of description we assume that they are stored as single files to be compressed: a file *av-t.raw* for raw *AV(t)*, a file *im-dc-s.img* for the last image $IM_{dc}(i,j,S)$, files *dc-0.dat*, *dc-2.dat* … *dc-15.dat* for data chains *DC(n)*, a file *descr.txt* that stores supplemental information – the number of images, image resolution and etc.

4.2 Lossless compression

There are a lot of software packages we can use for file compression. ZIP, TAR, RAR, UHA are the most famous of them. They differ from each other in internal compression algorithms and their implementations. To compress data obtained in previous step of our algorithm, we choose to apply the package ZIP due to its popularity, availability and high speed. Note that indeed any lossless compression package can be used instead of ZIP. The results of data compression are presented in Section 4.3. All obtained files *av-t.raw*, *im-dc-s.img*, *descr.txt*, *dc-0.dat* … *dc-15.dat* are compressed by the package ZIP to a single file. The decompression procedure is carried out in inverse order.

4.3 Compression results

The developed algorithm was also applied to pulsed thermography data measured by the testing system of Fraunhofer IZFP. The algorithm shows better compression ratio than pure ZIP

compression of the data in raw format. Table 3 summarizes the result of compression of two image sequences described in Section 3.3 (PVC plate with buried grooves (sample 1), polyethylene sample with flat bottom holes (sample 2)). As seen, the algorithm, namely the DCDT transformation, allows significantly to increase the compression ratio.

Table 3. Compression results on PVC and polyethylene sample

Sample	file size, MB		
	data in raw format (uncompressed)	ZIP compression	DCDT-ZIP compression
Sample 1	5.88	3.15	1.55
Sample 2	3.06	1.37	0.84

To complete the algorithm description, we note that the transformation DCDT should be adjusted to the compression package we apply. It concerns the last step (Eq. 6) when the data chains *DC(n)* are formed from $IM_{dc\text{-}sip}(i,j,t)$. Our tests have shown that, if ZIP is used, the transformation (Eq. 6) is useful, as it increases the compression ratio. But some packages (e. g. RAR in maximal compression mode) compress the data $IM_{dc\text{-}sip}(i,j,t)$ and *DC(n)* with almost the same ratios. So, the transformation (Eq. 6) can be skipped. Nevertheless, we emphasize that the DCDT transformation in the form we described is the most suitable and universal for any data or text compressor.

5. Conclusions and future work

In the present work, the new lossy and lossless compression algorithms for pulsed thermography data were proposed. The STM-JPEG algorithm combines a priori knowledge of the diffusion phenomena, the specific space/time representation of dynamically changing data and a well established static image compression algorithm. This combination achieves a high compression ratio while preserving high reconstruction quality. The DCDT-ZIP algorithm involves the specific transformation of dynamically changing data and a well established lossless data compression algorithm. The developed algorithms have demonstrated good results when applied to various experimental data sets measured by flash thermography.

Concerning further improvements, one can suggest for the STM-JPEG algorithm using 16-bit grey scale JPEG2000 compression. It will allow to preserve initial camera sensitivity (avoiding 256-level discretization) while forming the STM image.

REFERENCES

[1] RÖSNER (H.), NETZELMANN (U.), HOFFMANN (J.), KARPEN (W.), KRAMB (V.), MEYENDORF (N.). *Thermographic Materials Characterization.* In: Meyendorf N, Nagy P and Rokhlin S (eds.), Springer Series in Materials Sciences (Springer Verlag, New-York 2004) 247-285.

[2] *U. S. Patent 6,516,084*

[3] SHEPARD (S.M.), Ahmed (T.), RUBADEUX (B.A.), WANG (D.) and LHOTA (J.R.). *Synthetic Processing of Pulsed Thermographic Data for Inspection of Turbine Components.* In: Insight, Vol. 43 No. 9, Sept 2001, British Inst. of NDT, pp 587-589

[4] LUGIN (S.) and NETZELMANN (U.). *An effective compression algorithm for pulsed thermography data.* In: NDT&E International, Vol. 38, 2005, pp 485-490

[5] TAUBMAN (D.S.) and Marcellin (M.W.). *JPEG2000: Fundamentals, Standards and Practice.* Boston: Kluwer Academic Publishers, 2002.

[6] NELSON (M.) and GAILLY (J.). *The Data Compression Book.* New York: M&T Books, 1995.

Proc. Vth International Workshop, Advances in Signal Processing for Non Destructive Evaluation of Materials
Québec City (Canada),2-4 Aug. 2005. © X. Maldague ed., É. du CAO (2006), ISBN 2-9809199-0-X

Extraction of the Straight Line Segments from the Noisy Images as a Part of Pattern Recognition Procedure

by Andriy M. Chertov[1] and Roman Gr. Maev[1]

[1] *Centre for Imaging Research and Advanced Materials Characterization, University of Windsor, Ontario, N9B 3P4, Canada*

Abstract

The automated analysis of the images is of great importance today in many applications. In ultrasonic nondestructive evaluation of materials, the B- and C-scanning generates two-dimensional images which often require automated interpretation. Such images are often noisy and low-contrast. They are formed by combination of multiple ultrasonic waveforms obtained at different moments of investigation process or at different locations of the object of interest. The straight line segments are often formed on such images as a reflection of some physical phenomena taking place in the material. Such lines can sometimes be considered as the elements of more complex patterns when some a priory knowledge allows one to break the pattern into logical sub-elements. The suggested technique provides the way to recognize very low-contrast line segments on acoustical and other images when signal to noise ratio (SNR) is 1 and lower. At such SNR, the separation of real line from the noise artefacts becomes a challenging problem. The proposed technique provides the way of dealing with such problems by obtaining redundant amount of data from the area of interest using Radon transformation as the key part of the procedure.

Keywords: Radon transform, two-dimensional filter.

1. Introduction

Many two-dimensional images generated with ultrasonic and other testing techniques, images of the cities from the air etc. contain straight line pieces, or segments. On the airborne photos they represent the roads, channels and other artificial objects. On the images generated by the material testing equipment such lines could represent the physical processes or interfaces between contacting surfaces. As long as today's technology allows one to create an enormous amount of data related to the problem of interest, it is often impossible for a human to process it in the required time intervals. In many cases the interpretation of the image needs to be done within milliseconds after the image is acquired and a decision is to be made regarding the further actions. The processes need to be automated to deal with such situations. Today, in many applications, the computers are set up to automatically recognize the pattern on the image, interpret it and sometimes based on the interpretation to make an appropriate decision.

In many cases the straight line elements of possibly more complex patterns need to be extracted from the image to provide a physical, geometric or other interpretation of the image data. Often, such lines are hidden in the noise, overlap with other image elements. For example, Figure 1 presents a sub-image of the bigger image acquired during ultrasonic real-time testing of the resistance spot weld growth. The straight segment indicated with the arrow reflects the dynamics of the spot weld development and is a very important feature in the nugget quality characterization. The image is composed of multiple waveforms obtained during testing which lasts only tens of milliseconds [1, 2]. The intensity of the line is much lower than that of the other image elements which reduces the possibility to detect the line. Still, such straight lines possess the power the other picture elements do not have: these are the ordered structures. For such lines the Radon transform could be applied to detect their presence even when the SNR is very low. The original image can be pre-processed before doing the analysis but often the unwanted picture elements can not be removed completely. In noisy images the processing of the Radon transform itself is often required to have the opportunity to automatically detect the presence of the line of interest.

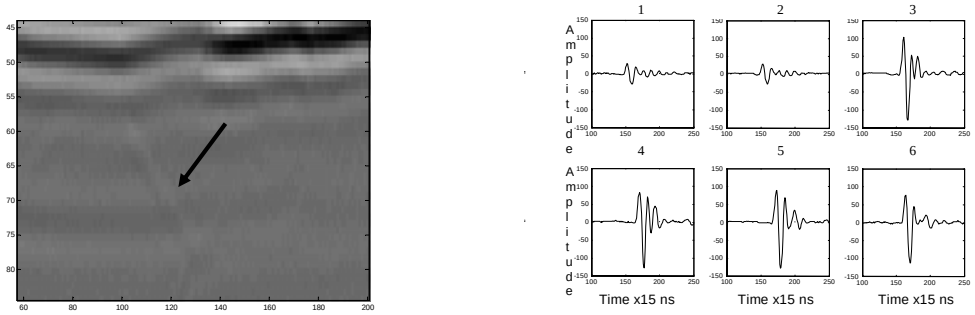

Figure 1. Example of the image with the straight line (left). The picture is the acoustical B-scan representing the dynamics of resistance spot weld growth. Every vertical line of the image is a separate oscillogram (right).

2. How the Radon Transform Works

If the image is gradually rotated around its center and projected on the fixed line, one will get a set of projections at different angles. The projections can be put together one after another to form a two-dimensional picture. On the x-axis there will be the degree of rotation, on the y-axis is the projection corresponding to that angle. **Erreur ! Source du renvoi introuvable.** shows the square with a straight line at 22 degrees with respect to the negative y-axis. Numerically, the black background of the image is composed of zeros and the line is composed of ones. Gradual rotation of this image clockwise around its center from 0 to 90 degrees and projection on the horizontal axis generates a Radon transform (RT) picture shown at **Erreur ! Source du renvoi introuvable.**. This transform shows a maximum at 22 degrees. Vertical axis is the projection whose length is $\sqrt{2}$ longer than the side of the square. The position of the maximum in Radon transform allows one to find the direction of the line (angle) in the image. Position at the projection axis (y-axis) defines the distance *D* of the line from the center of the image, see **Erreur ! Source du renvoi introuvable.**. Projection of the image on the horizontal line (plane of projection) in this figure creates one vertical line of data of the RT of **Erreur ! Source du renvoi introuvable.**. When image is rotated by angle β the transform will have a maximum corresponding to the strongest projection of the image line. Thus, the Radon transform can provide enough information to draw a line through the image along the discovered line.

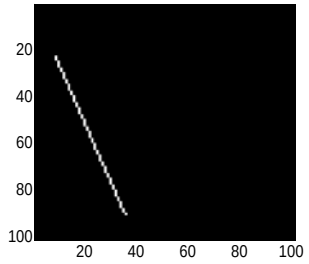

Figure 2. A 100x100 square with straight line at 22 degrees with respect to the -y-axis.

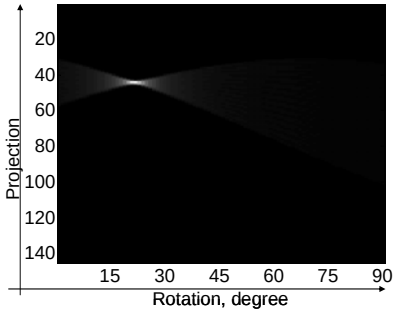

Figure 3. Radon transform of the image with projection peak at 22 degrees.

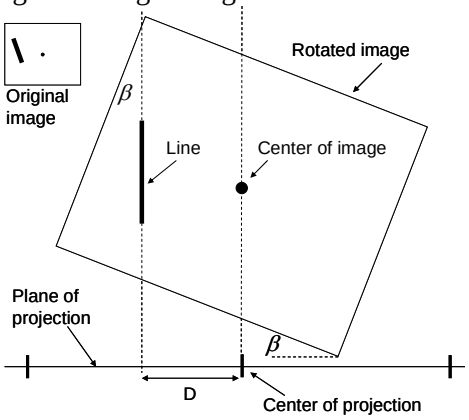

Figure 4. Image rotated by angle β.

The choice of the square (or rectangular) image is not the best one as long as the RT of the square is by its nature an uneven image, see Figure 5. Figure 6 shows the transform of the same square but with the line going through the square. In this case the original image is the same as in the **Erreur ! Source du renvoi introuvable.**, while numerically, the background is composed of ones and the line is composed of twos. On the Figure 6 the arrow shows the local maximum corresponding to the location of the line. But the center of the Radon image could be brighter as long as projection along the diagonal of the square (at 45 degrees) can easily exceed the amplitude of the line projection. The automatic peak (or maximum) detection could grab the

center of the image instead of the peak pointed with the arrow (the one we need to detect). To fight it the image can be made circular to have even amplitudes at any rotation angle, Figure 7, 8.

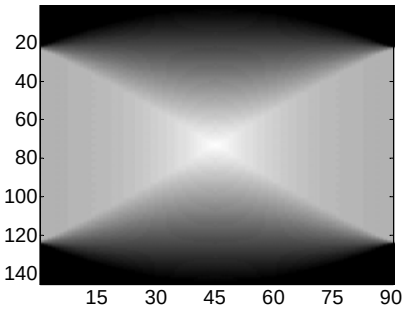

Figure 5. Radon transform of the even square of size 100x100.

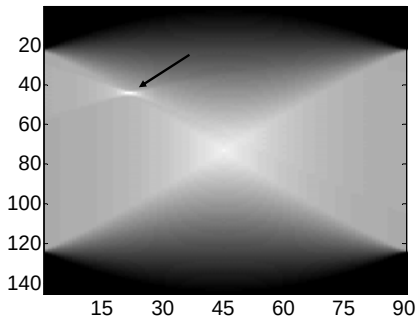

Figure 6. Radon transform of the even square with the straight line segment.

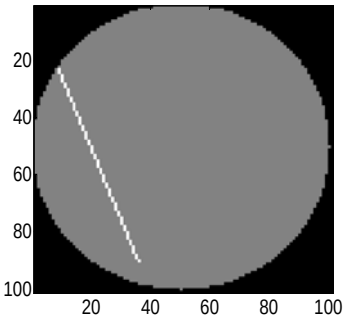

Figure 7. Line in the circular image.

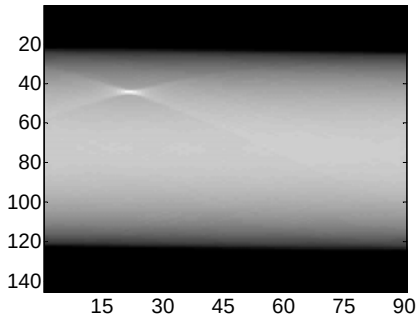

Figure 8. Radon transform of the circular image with the peak corresponding to the straight line at 22 degrees.

3. Transforms of the Noisy Images

The pictures shown in the previous section can be considered as examples for RT demonstration and present mostly academic interest. Such clear pictures with only a single straight element rarely happen in practice. In many practical applications, noises are an inalienable part of the image. In real images the signal to noise ratio could be of the order of 0.1-0.01. The lines of interest can be hidden in the more powerful signals. On Figure 9 one can see the circle with background modulated by sine function and a straight line of 0.2 of the sine amplitude. The corresponding RT is shown in Figure 10. In this case the picture becomes much more complicated for automatic analysis. There are a lot of local maxima, and their positions are unpredictable. If the amplitude of the line or its length slightly decreases the RT line peak will be below other local maxima. Its positioning will become an unreliable procedure.

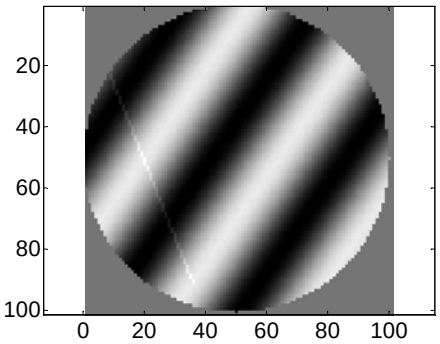

Figure 9. Circular image modulated by sine function and a line of 0.2 of the sine amplitude.

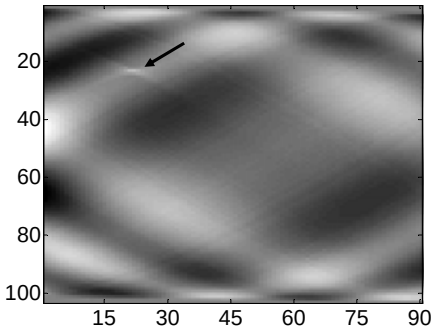

Figure 10. Radon transform of the image.

One of the possible solutions is filtering the RT image [3]. In many cases the peak of interest is smaller than other peaks and a 2-D high-pass filtering could be applied for the RT image. The choice of specific cutoff frequency is up to the application. For the given ultrasonic scans the following 2-D Remez filter was applied: order - 30; frequency response - [0 0.4 0.6 1] of Nyquist frequency corresponds to the amplitudes [0 0 1 1]. This is the high-pass filter with cutoff at 0.5 of the Nyquist frequency and the slope going from 0.4 Hz with zero response up to 0.6 Hz with unity response, see Figure 11. The result of filtering is shown at Figure 12. For comparison one can draw a vertical section of the RT image at 22 degrees – through the maximum. The upper plot of the Figure 13 shows the vertical image profile of the Figure 10 at 22 degrees; the lower plot is the vertical profile of the filtered image of the Figure 12. The arrows point at the peak of interest.

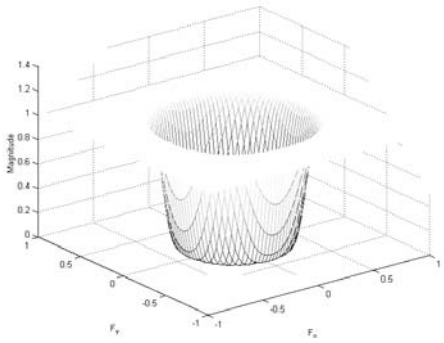

Figure 11. High-pass 2-D filter with 0.5 Nyquist cutoff frequency.

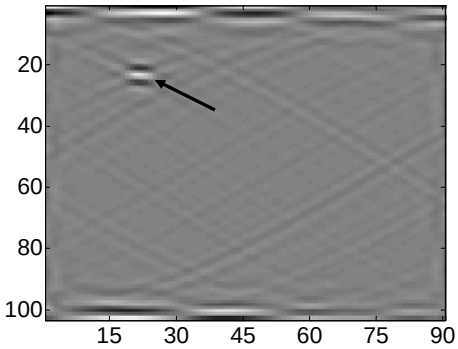

Figure 12. RT image filtered with high-pass filter.

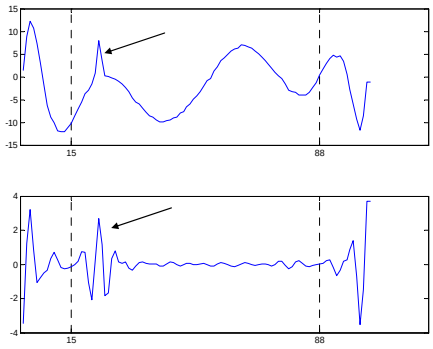

Figure 13. The vertical sections of the RT images at 22 degrees before (upper) and after (lower) filtering.

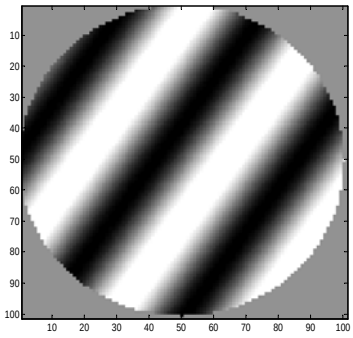

Figure 14. Circular image modulated by sine function and a line of 0.02 of the sine amplitude.

When the amplitude of the straight line is of the order of 1-5% of the noise amplitude, some additional processing is required for automatic location of the peaks. The image on the

Figure 14 has the line of 2% amplitude running the same way as in the previous, 20%, example. It can hardly be seen on the image. Still, the RT processing is capable to detect the line. On Figure 16 one can see the original RT image; the peak is too weak to be visualized. Figure 16 shows the results after the high-pass filtering .Now some weak "bump" can be recognized, and it is pointed to by the arrow. Still, the lines going approximately at 45 and -45 degrees are too strong. Such lines can be relatively easily removed using another 2-D filter with selective directional effect. Its action is aimed at removing the lines going approximately at +-45 degrees. The filter is shown at **Erreur ! Source du renvoi introuvable.**, and the result of its action on the previously filtered RT image is at the **Erreur ! Source du renvoi introuvable.**. The arrow points to the preserved and still detectable peak determining the location and orientation of the line segment on the original ultrasonic image. **Erreur ! Source du renvoi introuvable.** demonstrates the vertical profiles of the initial RT image, high-pass filtered and then selectively filtered ones - upper, middle and lower plots correspondingly. Even for the 2% amplitude the line can be successfully detected. **Erreur ! Source du renvoi introuvable.** shows the vertical sections of the RT images: original, high-pass filtered and diagonally filtered. The peak can be easily localized after the second filtering.

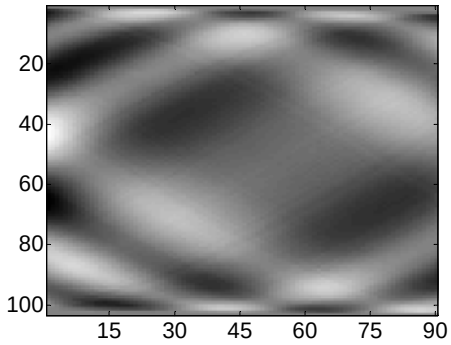

Figure 15. The unprocessed RT of the image with 2% intensity line.

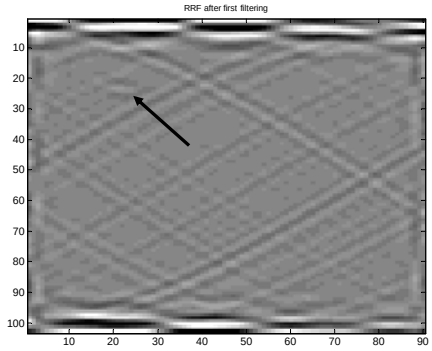

Figure 16. RT of the image with 2% line filtered with high-pass filter.

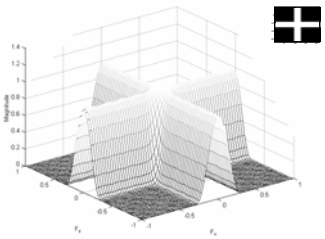

Figure 17. 3-D view of the second filter removing the near-diagonally oriented lines; small image in the right upper corner is a 2-D view of the same filter.

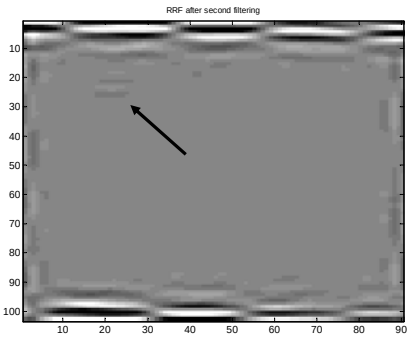

Figure 18. Results of the second filtering. Diagonal lines are removed while the useful information is preserved.

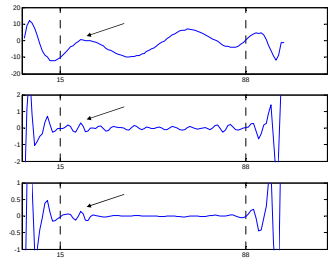

Figure 19. Image profiles of the original RT image (upper), high-pass filtered (middle) and diagonally filtered (lower) at 22 degrees. Arrow point at the place where the peak is located.

Also, studies have been made for the completely random images with line going the same way through the circular image. If the amplitude of the line is close to the random noise amplitude, the RT picture readily shows the location of the line, see Figure 20, 21. Here the line also goes at 22 degrees through the circle of random numbers and it can be seen easily. The RT picture also shows well defined spike indicated with the arrow. The situation is much worse when the line amplitude is 2-3 times lower than this. On Figure 22 one can barely see the presence of the line segment. The RT image of this circle is presented at Figure 24 and the global maximum is indicated by the arrow. This maximum will falsely define

the line position leading to erroneous interpretation of the original image. Looking at a pure RT image of the straight line (**Erreur ! Source du renvoi introuvable.**) one can see that the spike defining the line position is stretched horizontally. One could employ this fact to remove the noise in RT image in the horizontal direction using horizontal low-pass filter. The filter used to process the obtained RT image is shown at Figure 23. It removes high frequencies along the horizontal direction. In this case the global maximum is positioned at the right place defining the true position of the line in the image (Figure 25).

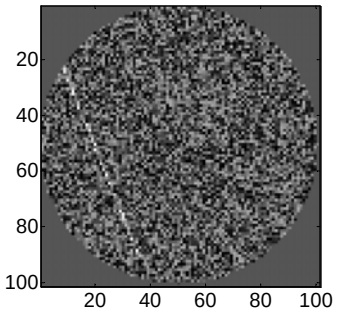

Figure 20. Line going through the circle of random numbers of amplitude in the range -0.5..+0.5. Line amplitude 0.5.

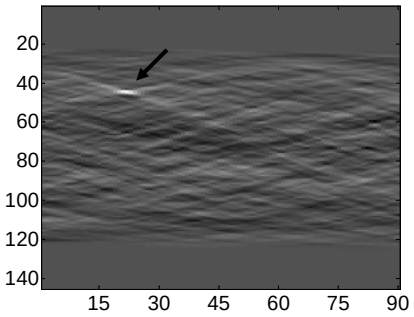

Figure 21. RT of the random image with line amplitude 0.5.

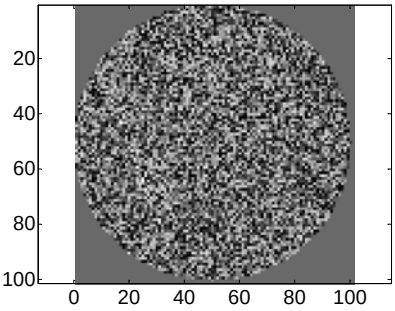

Figure 22. Line going through the circle of random numbers of amplitude in the range -0.5..+0.5. Line amplitude 0.2.

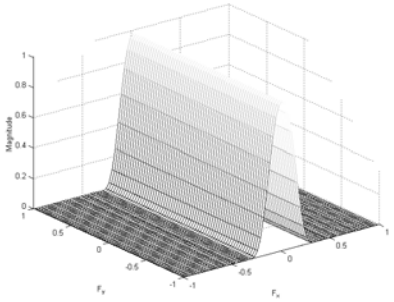

Figure 23. Horizontal low-pass filter.

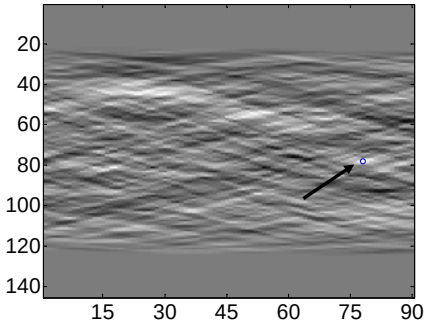

Figure 24. Original RT image with maximum in the "wrong" place.

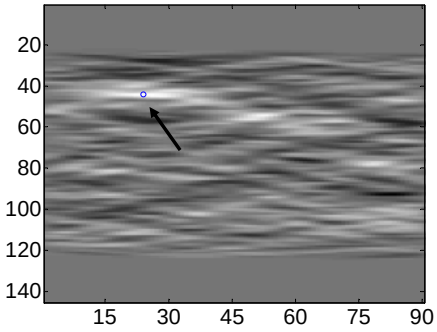

Figure 25. Horizontally filtered RT image reveals the true position of the line.

4. Conclusions

The automatic recognition of the patterns in the noisy images is a challenging task requiring a lot of efforts from the software developer. In cases when the patterns contain straight segments and their approximate position and/or orientation can be predicted, the Radon transform can significantly help define their position and orientation on the image. Preprocessing of the original image is the first thing which needs to be done before recognition process. Still, processing of the RT images is often required to be able to correctly localize the position of the lines of interest. In many cases the search of the peaks on the RT images do not need to be done in the range of 0..90 degrees. If the orientation of the line is approximately known the search can be run in the lower range of angles, thus looking for the local maximum instead of the global one. This also increases robustness of the technique eliminating the possibility to falsely grab some maximum due to the side effects of filtering on the edges of the RT image.

The choice of the filters for the RT images is defined by the nature of the image. In some cases the filtering is not required at all. But when the SNR is low, the RT image processing becomes a necessary task for developing robust techniques for line detection.

References

1. A.M. Chertov, R. Gr. Maev. “Inverse Problem Solution to Find Real-Time Temperature Distribution Inside the Spot Weld Medium Using Ultrasound Time of Flight Methods”, in *Quantitative Nondestructive Evaluation-2003.*
2. A.M. Chertov, R. Gr. Maev. “Determination of Resistance Spot Weld quality in Real Time Using Reflected Acoustic Waves. Comparison with Through-Transmission Mode.” 16th World Conference on Nondestructive Testing, August 30 – September 3, 2004, Montreal, Quebec.
3. Rafael C. Gonzalez, Richard E. Woods “Digital Image Processing”. Prentice Hall, Upper Saddle River, New Jersey 07458. ISBN 0-201-18075-8.

Proc. Vth International Workshop, Advances in Signal Processing for Non Destructive Evaluation of Materials
Québec City (Canada),2-4 Aug. 2005. © X. Maldague ed., É. du CAO (2006), ISBN 2-9809199-0-X

New Algorithm based on the Hough Transform for the Analysis of Pulsed Thermographic Sequences

D.A. González[a,b], C. Ibarra-Castanedo[b], J.M. López-Higuera[a], X. Maldague[b]

[a]Photonic Engineering Group, University of Cantabria,
ETSIIT - Avda. Los Castros s/n, 39005 Santander, Spain

[b]Computer Vision and Systems Laboratory, Université Laval,
Québec, Canada G1K 7P4
e-mail: dagonfer@teisa.unican.es

Keywords:

Pulsed Phase Thermography, Hough Transform, defect detection, defect characterization

Abstract

The automatic detection of subsurface defects has become one desired goal in the application of Non Destructive Techniques. A new algorithm based on the Hough Transform, is proposed to reduce human intervention to a minimum by Pulsed Thermographic. The final result provided by this algorithm is an image showing the different defects without having attended to parameters so determinant in other algorithms as the delayed time of the first image or any subjective point of view in the analysis.

Introduction

In recent years, Infrared Thermography (IT) has been extensively used in the Non Destructive Evaluation and Testing (NDT&E) scene. Although various methods have been developed around the world to improve and widen the use of IT[1], the human intervention is still necessary to interpret the thermographic sequences. Some previous works have given good results making the analysis of such sequences as independent as possible on the operator's point of view[2,3]. It is obvious that a priori knowledge of the specimen is fundamental most of the time. Nevertheless, in occasions it is sufficient to know whether the thermal decaying profiles at the surface can be modeled as a 1-D semi-infinite homogeneous sample or not. This fact helps to the analysis because the transient heat flow into the body can be quite well approximated by a simplification of the three-dimensional differential equation called Fourier diffusion equation[4]. This simplification characterizes the heat conduction in the body as a function, which relates linearly the logarithm of the temperature increase with the logarithm of the time that the process takes[5].

Let us consider the inspection of a semi-infinite homogeneous specimen under Pulsed Thermography (PT). The heat transfer at the surface follows a linear decay in a logarithmic space, approximating a -0.5 slope during all the inspection time for a non-defective or *sound* area, S_a. On the contrary, thermal decay for a defective area diverges from this behavior. In Figure 1, it is shown the different temporal histories for pixels belonging to defective and non-defective areas.

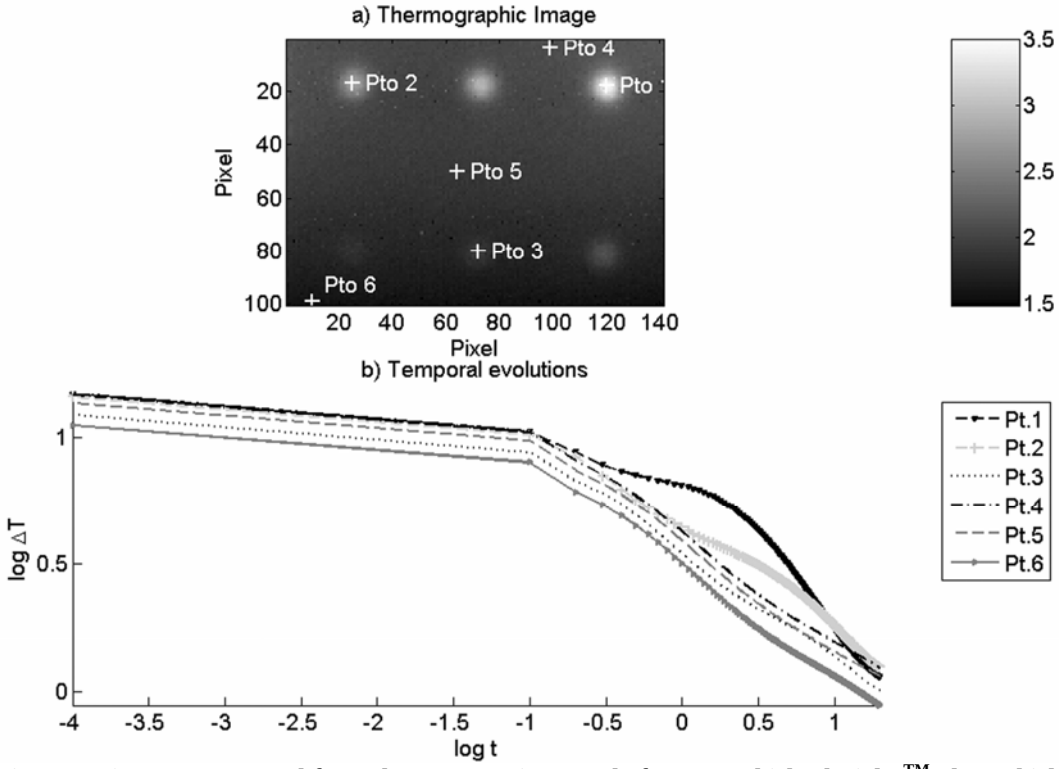

Figure 1. a) Image extracted from the sequence inspected of a 4 mm-thick Plexiglas™ plate which contains 6 10 mm-diameter flat-bottom circular-shaped holes (localized at depths: 1, 1.5, 2, 2.5, 3, 3.5 mm). b) Temporal evolution of contrast temperature for the selected points in a).

The analysis of a thermographic sequence for the detection of subsurface defects can be reduced to the identification of the -0.5 slope in the surface temperature decay for each pixel within the image. Using traditional techniques, which come from the field of computer vision[6], an algorithm can be developed in order to look for the -0.5 slope in the temporal temperature decay profiles of each pixel. Next sections resume the features of a new algorithm based on Hough Transform, which has been implemented to help in the analysis of thermographic sequences. Results for a Plexiglas™ specimen are also presented showing the independence on the subjectivity added by different operator's point of view.

Hough Transform in PPT

The Hough Transform (HT) is a standard tool in image analysis that allows recognition of patterns in an image space. Basically, this technique finds curves that can be parameterized like straight lines, polynomials, circles, etc., in a suitable parameter space[7]. The HT uses the parametric representation of a line:

$$\rho = x \cdot \cos\theta + y \cdot \sin\theta \qquad \textbf{eq. 1}$$

A pixel at coordinates (x,y) is transformed into the parameter space (ρ,θ) where the variable ρ is the distance from the origin to the line along a vector perpendicular to the line and θ is the angle between the x-axis and this vector. The HT generates a parameter space matrix whose rows and columns correspond to ρ and θ values respectively. Each point (x_i,y_j), with i,j=1,…,N , is transformed into sinusoidal curves in the (ρ,θ) plane, as

those shown in Figure 2. The intersection of all those curves shows the existence of a line in the image.

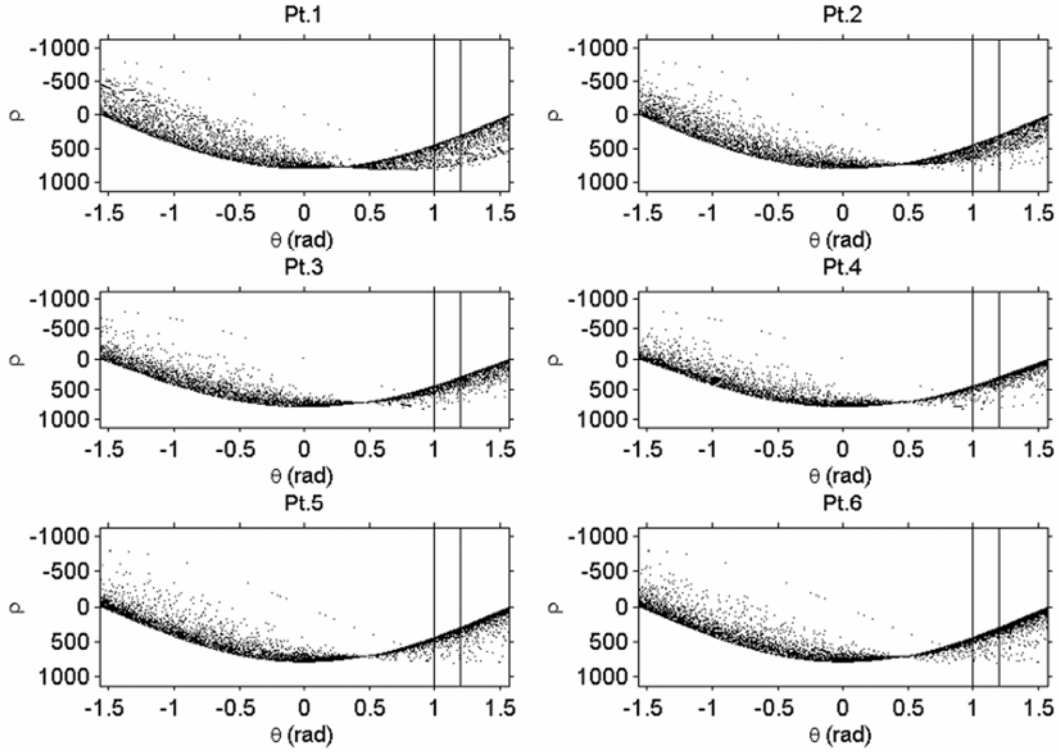

Figure 2. Parameter space (ρ,θ) for a) a free-defect area pixel b) defective area pixel. Curves are similar in both graphs but the curves spread more in the region 0.6<θ<0.7 for the graph b) because there are more points that do not belong to the same line.

However, assuming a semi-infinite homogeneous material, the goal is not to identify a line in the temporal profile of each pixel, which could be considered as a fitting or regression of data. The goal is to know if that pixel belongs to a defective or a non-defective area. Therefore, locating the number of points than follows a -0.5 slope makes the discrimination. From eq. 1, it can be deduced that the information resides in the column $\theta \approx 1.1071$ *rad.*

If all the points in the temporal history agree with a line of -0.5 slope, what should be seen in the Hough space is that all the curves intersect in only a point at the column $\theta \approx 1.1071$ *rad.* The coordinate ρ for that point will be the offset of the line. Otherwise, there are as many points in the column as lines with different offsets but the same -0.5 slope in the temporal history. Therefore, analyzing the distribution of the matches in that column selected above, it is possible to know if the pixel belongs to a non-defective area (sharp distribution) or if it belongs to a defective area (broad distribution, broader for deeper defects), as is shown in Figure 3.

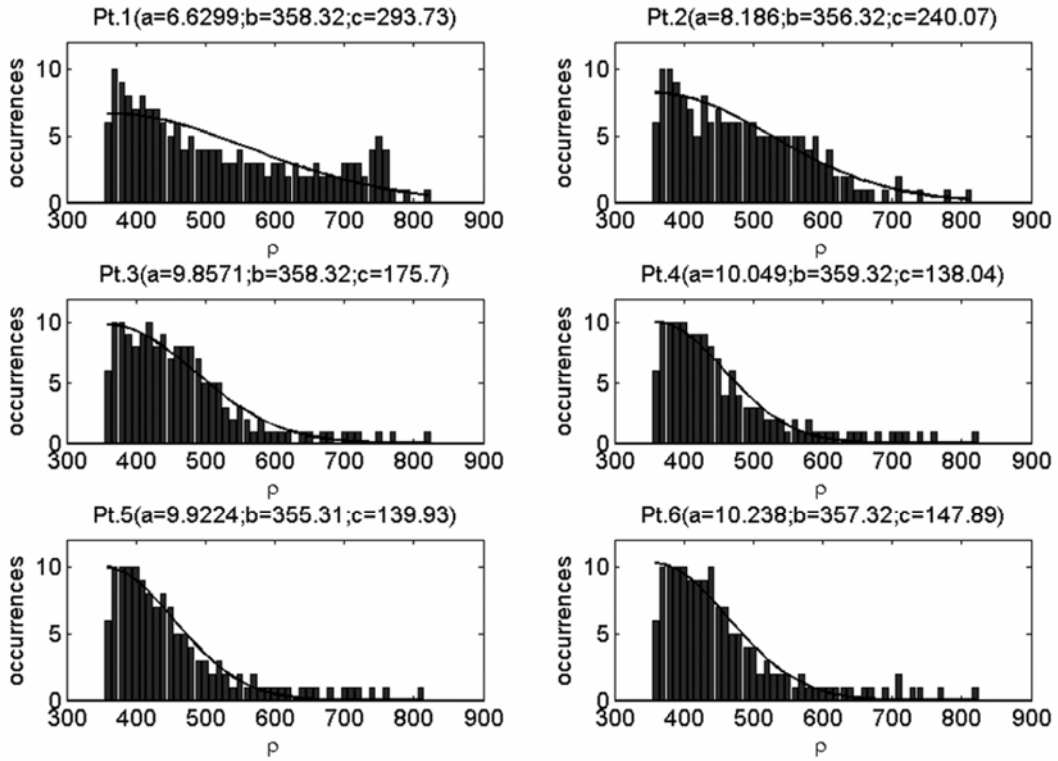

Figure 3. Histograms of values in column *θ≈1.1071 rad* for those pixels selected in Figure 1. In each graph the parameters of the fitting fit(x) = a*exp(-((x-b)/c)^2) are given.

Once the HT is applied to each pixel-temperature temporal history, the algorithm evaluates the obtained histograms and divides the pixels depending on the existence or not of the defects. In case that a defect is presented, the depth can be also estimated. Next section contains some of the results obtained using the algorithm together with a discussion about its benefits.

Experimental results

A 4 mm-thick Plexiglas^{TM} plate of dimensions 15x15 cm was stimulated during 15 ms using two photographic flashes (Balcar FX60). The sample contains 6 10 mm-diameter flat-bottom circular holes localized at different depths (1, 1.5, 2, 2.5, 3, 3.5 mm), see Figure 1. 200 thermograms (from t=0.1 to t=20 s) were recorded after the heating pulse using a Santa Barbara focal plane infrared camera, model SBF125.

Processing of the sequence with the Pulse Thermography Hough Transform Algorithm (PTHTa) it is possible to get results that agree with those obtained through other methodologies shown in Figure 4.

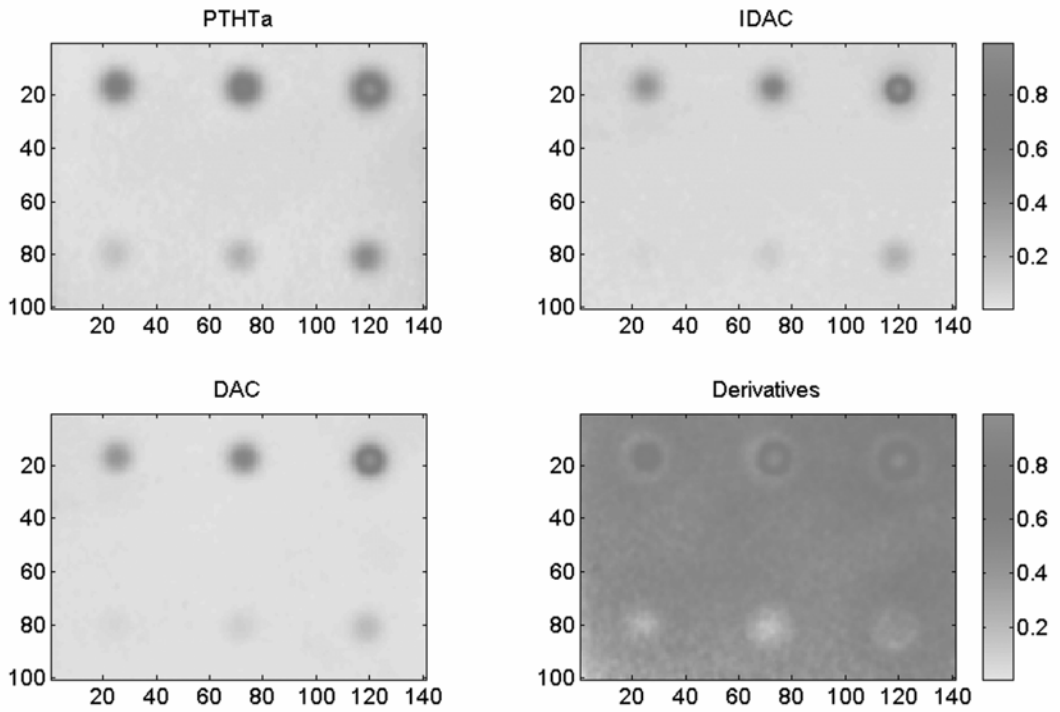

Figure 4. A comparative among different methods of analysis of thermographic sequences is shown. Best contrast images for: a) PTHTa algorithm, here presented b) IDAC algorithm[3] c) DAC method[5] d) First and second derivatives[8].

Although this algorithm is computationally expensive, it provides better-quality contrast images than other algorithms such as IDAC algorithm[3], DAC method[5] or the first and second derivatives[8]. For example, the deepest defect is visible by PTHTa while this is not possible by the IDAC method (previous automated algorithm presented by the authors[3]). Diffusion is higher at the defects' edges of the as can be seen in the Figure 4, but not as high as the diffusion levels observed with the derivatives method. Furthermore, computing the two-dimensional correlation coefficient between the obtained contrast images, values of 0.93 are achieved. The information according to depth is maintained and also the color scale presents a good correlation with depth as can be seen in Figure 5.

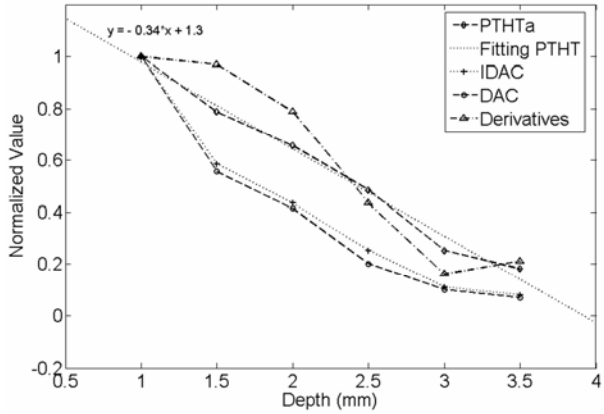

Figure 5. The normalized value of the color scale for each defect on the graphs within Figure 4 is printed versus the depth of the defect. The new PTHT algorithm herein presented shows the best linear behaviour.

PTHTa makes possible the elimination of errors due to different operator's point of views and so, represents better capabilities in the assessment of specimens. Besides, the selection of a sound area, necessary in most thermographic post processing techniques, is eluded due to be based in a 1-D model. This situation also helps to reduce non-uniformities dues to the heating source, a common problem in active thermography. The influence of the initial time of acquisition, which is a source of incertitude to the measurement and a high non linearity in the log representation of the temporal decay, also is avoided thanks to the fact that dispersed data are not so representative in an algorithm based on occurrences. Therefore, an algorithm absolutely free of human decisions is herein presented.

Conclusions

A new algorithm based on the Hough Transform is proposed for the analysis of Pulsed Thermographic sequences. The Pulsed Thermography Hough Transform algorithm (PTHTa) provides contrast images free of subjectivity associated with human intervention and avoids the necessity of defining a sound area and establishing the initial time of acquisition. Besides, all the information is contained in just one image and leading to a quantitative estimation of the defect depths. Specimens under inspection should be semi-infinite homogeneous samples because this algorithm is supported on a 1-D Fourier diffusion equation approximation. Experimental works using a Plexiglas^{TM} specimen were realized showing a good agreement with other semi-automated techniques.

Acknowledgments

The Spanish Science and Technology Minister under project SiRAS TEC2004-05936-C02-02 and the Natural Sciences and Engineering Research Council of Canada have supported this work.

References

[1] X. Maldague, Theory and Practice of Infrared Technology for NonDestructive Testing. , John Wiley-Interscience (2001) p. 684.
[2] D.A. González, C. Ibarra-Castanedo, F.J. Madruga, X. Maldague, Differentiated Absolute Phase Contrast Algorithm for the Analysis of Pulsed Thermographic Sequences, submitted to Infrared Physics & Technology.
[3] D.A. González, C. Ibarra-Castanedo, M. Pilla, M. Klein, J.M. López-Higuera, X. Maldague, Automatic Interpolated Differentiated Absolute Contrast Algorithm for the Analysis of Pulsed Thermographic Sequences, Proceedings of 7th International Conference on Quantitative Infrared Thermography (QIRT'04), 2004
[4] H.S. Carlslaw, J.C. Jaeger, Conduction of Heat in Solids, Oxford University Press, 2nd edition, 1959.
[5] M. Pilla, M. Klein, X. Maldague, A. Salerno, "New Absolute Contrast for Pulsed Thermography ", Proceedings of QIRT 2002, D. Balageas, G. Busse, G. Carlomagno eds.
[6] W K. Pratt, Digital Image Processing. , Wiley, New York (1991) p. 698.
[7] J.C. Russ, The Image Processing Handbook (2nd Edition), CRC Press, Florida (1995), p 674.
[8] R. E. Martin, A. L. Gyekenyesi, S. M. Shepard, "Interpreting the Results of Pulsed Thermography Data," Materials Evaluation, 61[5]: 611-616, 2003.